Ionization dynamics of C_2H_2 in intense laser fields: Time-dependent Hartree-Fock approach

Shi-Lin Hu,[1,2] Zeng-Xiu Zhao,[3,*] Jing Chen,[1,4,†] and Ting-Yun Shi[2,‡]

[1]*Institute of Applied Physics and computational Mathematics, P.O. Box 8009, Beijing 100088, China*

[2]*State Key Laboratory of Magnetic Resonance and Atomic and Molecular Physics, Wuhan Institute of Physics and Mathematics, Chinese Academy of Sciences, Wuhan 430071, China*

[3]*Department of Physics, National University of Defense Technology, Changsha 410073, China*

[4]*HEDPS, Center for Applied Physics and Technology, Peking University, Beijing 100084, China*

(Received 6 August 2015; published 9 November 2015)

We investigate the multielectron ionization dynamics of C_2H_2 subjected to intense few-cycle laser fields with the time-dependent Hartree-Fock approach, in which one-center method is employed with the finite-element discrete-variable representation and B-spline functions. It is found that, when the photon energy is close to the energy gap between the two inner orbitals, an inner-orbital single-photon resonant transition phenomenon occurs and plays an important role in the ionization process of the molecule. Furthermore, the ionization of inner electrons surpasses that of the electrons in the highest occupied molecular orbital (HOMO) at high laser intensities, which may be attributed to the effect of the spatial distributions of molecular orbitals. Moreover, this phenomenon will be enhanced by a reduction of the screen for electrons in the HOMO due to the ionization of inner electrons.

DOI: 10.1103/PhysRevA.92.053409 PACS number(s): 33.80.Rv, 42.50.Hz, 42.65.Re

I. INTRODUCTION

The investigation of multielectron dynamics in strong laser fields has been widely carried out experimentally for the ionization of atoms and molecules [1], which is partly triggered by the advancement in short-pulse and high-power laser technology. For example, the time-resolved Auger effect of the krypton atom has been measured in a pump-probe experiment with a femtosecond visible light pulse and a subfemtosecond soft-x-ray pulse [2], which provides us with physical insights into the ultrafast atomic dynamics. The attosecond streaking measurements reveal a delay of 21 ± 5 as ($1\ \text{as} = 10^{-18}$ s) for the electron released from the $2p$ orbital relative to that liberated from the $2s$ orbital of Ne [3]. For molecules, it was found that the low-lying orbitals, as well as the highest occupied molecular orbital (HOMO), play an important role in the tunnel ionization for HCl and CO_2 [4,5]. Recently, the carrier-envelope phase (CEP) effect was shown to be crucial in ultrashort laser pulses and the CEP-effect-dependent ionization of polyatomic hydrocarbon and carbon disulfide molecules has been investigated [6,7].

Regarding the theoretical aspect of multielectron dynamics, considerable effort has been devoted to the direct solutions of the Schrödinger equation for two-active-electron atoms and molecules. One common method of doing this is to take into account the motion for each electron in one spatial dimension and introduce soft Coulomb parameters to deal with the singularities of the Coulomb potential [8–10]. Double ionization of He has been investigated by the reduced-dimensional model atom and Coulomb-repulsion-assisted laser acceleration effects come into play in the nonsequential double-ionization process [11]. Meanwhile, the one-dimensional model has also been applied to study enhanced ionization of the hydrogen molecule in an intense laser field [12]. Another method is to obtain the solutions of the Schrödinger equation for three-dimensional systems by direct numerical integration [13,14]. Benchmark results of multiphoton ionization for He have been obtained by combining finite-difference grids with partial-wave expansion [15]. Enhanced ionization of the H_2 molecule has been studied based on the Laguerre and Legendre polynomials in spheroidal coordinates [16]. However, the full-dimensional calculation with two active electrons is still a challenge.

It is well known that the full *ab initio* computational tasks involving more than two electrons are tremendous, so affordable approaches that retain a fully quantum mechanical picture have been proposed to overcome this difficulty. One such approach is the time-dependent density-functional theory (TDDFT) [17–19]. In the TDDFT, a local exchange-correlation potential is introduced to account for the correlation effect. However, the consequence is that the results show a dependence on the exchange-correlation potential since the exchange-correlation function is unknown [20]. Another approach is the time-dependent Hartree-Fock (TDHF) theory, which has attracted a great attention because it is not expensive for complex systems and takes into account the response of all electrons in strong laser fields [21]. In strong-field atomic and molecular physics, the TDHF method is used to study the multiphoton ionization dynamics of the helium atom in an intense laser field [22], in which the orbitals of two electrons are the same and electron correlation is not well described. Later, an unrestricted Hartree-Fock method was developed to account for the correlation effect to some extent, in which the two electrons reside in different orbitals [9,23,24]. However, all of the above-mentioned works focus on few-body systems, e.g., He or H_2, exposed to intense laser fields. The multielectron dynamics of ethene, benzene, and the formaldehyde cation have been calculated with the TDHF theory based on Gaussian basis sets, however the approach could not describe the ionization behavior accurately due to the local character of Gaussian functions [25]. Recently, the

*zhao.zengxiu@gmail.com
†chen_jing@iapcm.ac.cn
‡tyshi@wipm.ac.cn

mechanism of efficient ionization for C_2H_2 was studied by a one-dimensional model and it was shown that the electrons are ejected through tunneling after being transferred to the proton positions [26,27]. Compared with the one-dimensional model, the energies of the HOMO and the HOMO-1 are not nearly degenerate and some differences exist for enhancing ionization phenomena with respect to three-dimensional system [28], so it is necessary to develop a TDHF approach to study the three-dimensional system subjected to intense laser pulses. In addition, the impact of inner electrons on ionization behavior needs to be studied further, which has led to increasing interest recently [29–31]. In Refs. [29,30] it was found that the polarization of the core plays an important role in the molecular alignment-dependent ionization and photoelectron cutoff energy. In Ref. [31] it was shown that dynamical antiscreening has a significant effect on the ionization behavior in the single-photon regime.

The goal of the present paper is to extend our previous works [32,33] to investigate the effect of inner electrons on the ionization dynamics of C_2H_2 in intense few-cycle laser fields with the TDHF approach, in which the one-center method is combined with the finite-element discrete-variable representation (FEDVR) and B splines. There are two advantages. First, the FEDVR could properly describe the long-range wave function and efficiently calculate two-electron integrals [34–37]. Second, B splines could appropriately handle electron-nucleus cusps [32,38,39]. The outline of the present work is as follows. In Sec. II we describe the TDHF calculations carried out with FEDVR bases, B splines, and the Crank-Nicolson method. Our results and a discussion are presented in Sec. III. A summary and outlook are given in Sec. IV.

II. THEORETICAL METHODS

Within the dipole approximation, the TDHF equations for linear molecules could be written as (atomic units are used in this paper unless indicated otherwise) [26–28]

$$i\frac{\partial}{\partial t}\Psi_i(\mathbf{r},t) = [H_1(\mathbf{r}) + 2J(\mathbf{r},t) - K(\mathbf{r},t) - \mathbf{r}\cdot E(t)]\Psi_i(\mathbf{r},t). \tag{1}$$

For a given magnetic quantum number m, the one-electron Hamiltonian of $H_1(r)$ is

$$H_1(\mathbf{r}) = -\frac{1}{2r^2}\frac{\partial}{\partial r}r^2\frac{\partial}{\partial r} + \frac{1}{2r^2}\left(\frac{\partial}{\partial \xi}(1-\xi^2)\frac{\partial}{\partial \xi} - \frac{m^2}{1-\xi^2}\right) - \frac{Z_a}{|\mathbf{r}-\mathbf{R}_1|} - \frac{Z_a}{|\mathbf{r}+\mathbf{R}_1|} - \frac{Z_b}{|\mathbf{r}-\mathbf{R}_2|} - \frac{Z_b}{|\mathbf{r}+\mathbf{R}_2|}, \tag{2}$$

where $\xi = \cos\theta$ and $Z_a = 1$ and $Z_b = 6$ are the charges of the H nucleus and C nucleus, respectively. Internuclear distances $R_1 = 4.138$ a.u. and $R_2 = 1.138$ a.u. are assumed in the present study. Figure 1 shows the coordinates of the C_2H_2 molecule. The potential terms are expanded by Legendre polynomials as

$$\frac{1}{|\mathbf{r}\pm\mathbf{R}|} = \sum_{\lambda=0}^{\lambda_{\max}}(\pm)^\lambda\frac{r_<^\lambda}{r_>^{\lambda+1}}P_\lambda(\xi), \tag{3}$$

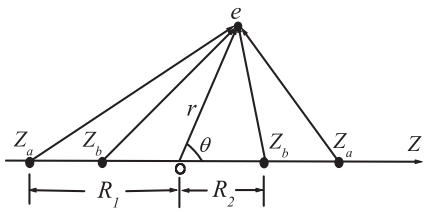

FIG. 1. Coordinates of the C_2H_2 molecule.

where $r_<$ ($r_>$) corresponds to $\min(r,R)$ [$\max(r,R)$] and $P_\lambda(\xi)$ are the Legendre polynomials. We set $\lambda_{\max} = 200$ in our work. Here $J(r,t)$ and $K(r,t)$ indicate the electron-electron Coulomb interaction and the electron-electron exchange interaction, respectively,

$$J(\mathbf{r}_1,t)\Psi_i(\mathbf{r}_1,t) = \sum_j^N\int\frac{|\Psi_j(\mathbf{r}_2,t)|^2}{\mathbf{r}_{12}}d\mathbf{r}_2\Psi_i(\mathbf{r}_1,t) \tag{4}$$

and

$$K(\mathbf{r}_1,t)\Psi_i(\mathbf{r}_1,t) = \sum_j^N\int\frac{\Psi_j^*(\mathbf{r}_2,t)\Psi_i(\mathbf{r}_2,t)}{\mathbf{r}_{12}}d\mathbf{r}_2\Psi_j(\mathbf{r}_1,t), \tag{5}$$

where N is the number of occupied orbitals and the two-electron interaction operator could be written in the formula

$$\frac{1}{\mathbf{r}_{12}} = \frac{1}{r_>}\sum_{l=0}^{l_{\max}}\frac{r_<^l}{r_>^l}P_\lambda(\cos\theta_{12}) = \sum_{l=0}^{l_{\max}}\sum_{m=-l}^{l}\frac{(l-|m|)!}{(l+|m|)!}\frac{r_<^l}{r_>^{l+1}}P_l^{|m|}(\xi_1)P_l^{|m|}(\xi_2)e^{im(\varphi_1-\varphi_2)}. \tag{6}$$

Here $r_>$ ($r_<$) is the bigger (smaller) of r_1 and r_2 and $P_l^{|m|}(\xi_1)$ are associated Legendre polynomials ($l_{\max}$ is 25). The laser field is linearly polarized along the molecular axis and the vector potential is $A(t) = \frac{E_0}{\omega}\sin^2(\frac{\pi t}{t_{\max}})\cos\omega t$, $0 < t < t_{\max}$, where E_0 is the peak electric field and $t_{\max}$ and ω are the duration and the frequency of the laser pulse, respectively. The time-dependent electric field is defined via the vector potential $A(t)$ as $E(t) = -\frac{\partial}{\partial t}A(t)$.

As described above, the electron-electron interactions are time dependent in the TDHF theory, so it is necessary to efficiently calculate two-electron integrals. It is shown that Gaussian functions quickly evaluate the two-electron integral, but they cannot describe the asymptotic wave function properly [40,41] as an electron could be found far from the core in the strong laser field. The FEDVR basis is adjustable, so it could represent both bound states and continuum states reasonably well, which is important to describe physical phenomena in the intense laser field. In addition, it has been established that the FEDVR is highly efficient and accurate in performing two-electron integral calculations [34–36]. Consequently, the wave functions in the present study are expanded in terms of

the FEDVR and B splines as

$$\Psi_i(r,\xi,\varphi,t) = \frac{1}{\sqrt{2\pi}} \sum_{\mu\nu} C^i_{\mu\nu}(t) \frac{\chi_\mu(r)}{r} B^k_\nu(\xi)(1-\xi^2)^{|m|/2} e^{im\varphi}. \tag{7}$$

Gauss-Lobatto quadrature points are adopted in the radial direction to construct DVR basis functions and the first and last basis functions are removed due to the boundary condition. Dense finite elements are distributed near the core to properly describe the bound states and evenly spaced finite elements are employed at a large distance to appropriately describe the continuum states. Each FEDVR $\chi_\mu(r)$ contains a DVR of order 10; the details of the FEDVR could be found in Refs. [34,37]. The angular wave function is expressed with B splines to properly cope with electron-nucleus cusps and $B^k_\nu(\xi)$ is the B spline of order $k = 7$ [42]. The factor $(1-\xi^2)^{|m|/2}$ could describe the wave function well for ξ close to ± 1. At $t = 0$, we obtain the occupied and unoccupied orbitals by Hartree-Fock calculations [32,33], in which the radial parts of the two-electron integrals are calculated by solving Poisson's equations [37].

We solve Eq. (1) using the Crank-Nicolson method [42] and the orthogonality of different orbitals is enforced during the time propagation [27]. A $\cos^{1/8}$ absorber function is used in a range from $r = r_{\max} - 14$ a.u. to $r_{\max}$ to avoid spurious reflection. After obtaining the time-dependent wave functions $\Psi_i(r,\xi,\varphi,t)$, the time-dependent probability for the electron ionized from the i orbital is expressed as

$$P_i(t) = 1 - \langle \Psi_i(\mathbf{r},t) | \Psi_i(\mathbf{r},t) \rangle. \tag{8}$$

Here $P_S(t) = \sum_i P_i(t)$ is the total ionization probability for the electron removed from the occupied orbitals. The component of the j field-free orbital contained by the n time-dependent orbital is defined as

$$P_{jn}(t) = |\langle \Psi_j(\mathbf{r},t=0) | \Psi_n(\mathbf{r},t) \rangle|^2 \tag{9}$$

and the i orbital energy during time propagation is written as

$$\varepsilon_i(t) = \langle \Psi_i(\mathbf{r},t) | H_1(\mathbf{r}) + 2J(\mathbf{r},t) - K(\mathbf{r},t) | \Psi_i(\mathbf{r},t) \rangle. \tag{10}$$

In the present paper the total pulse duration is three optical cycles and the time step is 0.02 a.u. Eighty-nine FEDVR bases and 14 B splines are employed; the radial domain $r_{\max} = 30$ a.u. is adopted for numerical calculations. We also perform calculations for $r_{\max} = 40$ a.u. and the absorber function in a range from $r = r_{\max} - 10$ a.u. to $r_{\max}$ and the convergence of $P_i(t)$ and $\varepsilon_i(t)$ at the end of the pulse is reached within 8%.

III. RESULTS AND DISCUSSION

The orbital energies of C_2H_2 are tabulated in Table I at the Hartree-Fock level and the reference values are obtained from cc-pvQZ basis sets [43]. As one can see, our results are in reasonable agreement with the reference data. For the inner shells $1\sigma_g$ and $1\sigma_u$, the discrepancies of our data with the reference values are somewhat larger but still within 1%. Because the binding energies of the $1\sigma_g$ and $1\sigma_u$ orbitals are much larger than those of other orbitals, the $1\sigma_g$ and $1\sigma_u$ orbitals are assumed to be frozen, interacting with the laser field. In the present work we adopt $P_S(t) = \sum_i P_i(t)$, $i = 2\sigma_g, 2\sigma_u, 3\sigma_g, 1\pi_u$. The charge distribution of the $2\sigma_g$, $2\sigma_u$, $3\sigma_g$, and $1\pi_u$ orbitals is plotted in Fig. 2. For the $2\sigma_g$ and $2\sigma_u$ orbitals, the electron clouds are mostly localized near C nuclei. For the $3\sigma_g$ orbital, the orbital density is distributed much evenly around C and H nuclei with regard to $2\sigma_g$ and $2\sigma_u$ shells. For the $1\pi_u$ orbital, the electron cloud is symmetrically distributed near C nuclei and no charge distribution is located along the molecular axis compared with σ orbitals.

TABLE I. Comparison of orbital energies (in a.u.) for internuclear separations $R_1 = 4.138$ a.u. and $R_2 = 1.138$ a.u.

Orbitals	Present work	Ref. [44]
$1\sigma_g$	−11.2042	−11.2724
$1\sigma_u$	−11.2008	−11.2688
$2\sigma_g$	−1.0084	−1.0123
$2\sigma_u$	−0.6023	−0.6026
$3\sigma_g$	−0.5308	−0.5291
$1\pi_u$	−0.4043	−0.4041

A. Laser field: 800 nm

Figure 3 shows the probability for the electron ionized from the i orbital $P_i(t)$ and the total ionization probability $P_S(t)$ with an increase of the peak electric field from $E_0 = 0.02$ to 0.08 a.u. for the 800-nm central wavelength; I indicates the laser intensity. In general, the probabilities for the electrons removed from occupied orbitals and the total ionization probability increase with laser intensity. However, a closer inspection reveals some intriguing physical phenomena in Fig. 3.

In Fig. 3 the ionization probability of the electron removed from the $2\sigma_u$ orbital (HOMO-2) is close to that from the $3\sigma_g$ orbital (HOMO-1) at the end of the pulse, though the electron is bound more tightly in the HOMO-2 than in the HOMO-1 (see Table I). In general, the ionization behavior of the electrons is mainly determined by the following factors: (i) the binding energy of the orbital (the more tightly bound, the smaller the ionization probability), (ii) the multiphoton resonant effect (which gives rise to an increase of the ionization probability), and (iii) the charge distribution of the corresponding orbital (if the electron cloud is parallel to the direction of laser

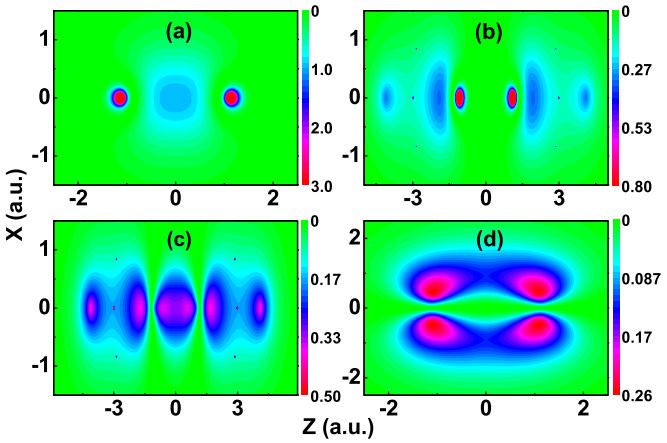

FIG. 2. (Color online) Orbital densities (arbitrary units): (a) $2\sigma_g$, (b) $2\sigma_u$, (c) $3\sigma_g$, and (d) $1\pi_u$.

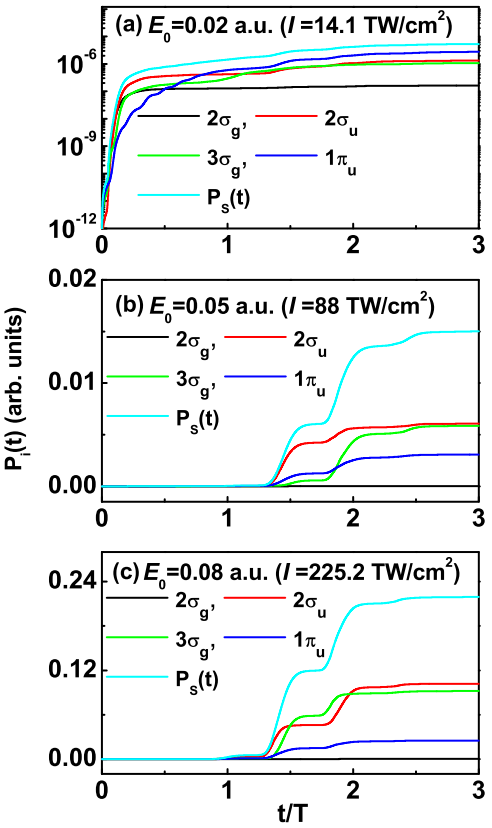

FIG. 3. (Color online) Probabilities of the electron ionized from the i shell $P_i(t)$ and the total ionization probability $P_S(t)$ with an increasing 800-nm laser field ($T = \frac{2\pi}{\omega}$). Note that the probabilities are plotted in logarithmic form in (a). For visual convenience, the curves in (b) and (c) are depicted in linear form and the ionization starts at $t = 0$.

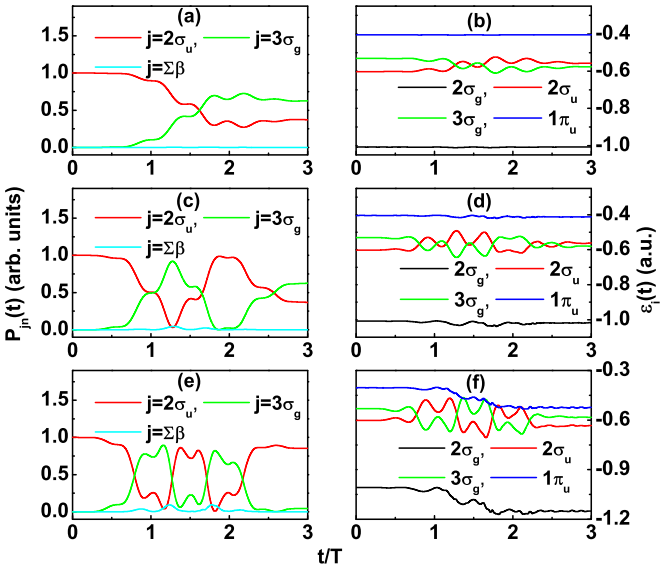

FIG. 4. (Color online) Plot of $P_{jn}(t)$ and orbital energies $\varepsilon_i(t)$ with an increasing 800-nm laser field: (a) and (b) $E_0 = 0.02$ a.u. ($I = 14.1$ TW/cm^2), (c) and (d) $E_0 = 0.05$ a.u. ($I = 88$ TW/cm^2), and (e) and (f) $E_0 = 0.08$ a.u. ($I = 225.2$ TW/cm^2). Note that $n = 2\sigma_u$ in (a), (c) and (e) and the cyan curve indicates the sum of the projection of $\Psi_{2\sigma_u}(\mathbf{r},t)$ on field-free unoccupied σ orbitals (see the text).

polarization, it is easy to detach the electron). In Fig. 3 the ionization probability of the $2\sigma_g$ electrons is small because of the large ionization energy in Table I. In addition, the ionization probability of the $2\sigma_u$ electrons is analogous to that of the $3\sigma_g$ electrons at the end of the pulse. This is because the photon energy is $\omega = 0.057$ a.u. (800 nm), which is close to the energy separation $\Delta E = 0.07$ a.u. between the $2\sigma_u$ and $3\sigma_g$ shells in Table I and hence a single-photon resonant transition between the $2\sigma_u$ and $3\sigma_g$ orbitals can occur. To further gain physical insights into the change of the ionization probabilities for the electron in occupied orbitals with increasing laser fields, we depict the projection of the time-dependent orbitals $\Psi_{2\sigma_u}(\mathbf{r},t)$ (HOMO-2) on the field-free HF orbitals ($2\sigma_u$ and $3\sigma_g$) in Figs. 4(a), 4(c), and 4(e), where the cyan curve denotes the sum of probabilities of field-free unoccupied σ orbitals in $\Psi_{2\sigma_u}(\mathbf{r},t)$ (β ranges from the first unoccupied σ orbital to the 20th unoccupied σ orbital). The time-varying orbital energies for all occupied time-dependent orbitals are shown in Figs. 4(b), 4(d), and 4(f) as well. It can be seen that there is much stronger mixing between time-independent orbitals $\Psi_{2\sigma_u}$ and $\Psi_{3\sigma_g}$ in $\Psi_{2\sigma_u}(\mathbf{r},t)$ in Figs. 4(a), 4(c), and 4(e), which can also be found in Ref. [28]. However, it is different from the enhanced excitation due to the stronger mixing among field-free $1\sigma_g$ and $1\sigma_u$ states for H_2^+ subjected to intense laser fields in Refs. [44,45] because the $1\sigma_g$ and $1\sigma_u$ shells are the HOMO and the lowest unoccupied molecular orbital for H_2^+, respectively.

As the peak field strength increases from 0.02 to 0.08 a.u., it is found in Figs. 4(c) and 4(e) that the populations for $2\sigma_u$ and $3\sigma_g$ are oscillating at higher frequency, which closely resembles the Rabi oscillation with the frequency dependent on the laser field strength [46]. For the case of $E_0 = 0.08$ a.u., the population of $3\sigma_g$ is small at the end of the pulse in Fig. 4(e), which is accidental due to the Rabi oscillation. We have carried out additional calculations for the field with two or four optical cycles and the population of $3\sigma_g$ is not small at the end of the pulse. In addition, as the laser field increases, the populations of $2\sigma_u$ and $3\sigma_g$ in $\Psi_{2\sigma_u}(\mathbf{r},t)$ in Figs. 4(a), 4(c), and 4(e) show a more complex dynamics because $2\sigma_u$ and $3\sigma_g$ states can also couple with other unoccupied orbitals. As shown in Fig. 5, the sum of the population of unoccupied orbitals such as $3\sigma_u$ and $4\sigma_g$ in $\Psi_{2\sigma_u}(\mathbf{r},t)$ (the cyan curve) begins to intersect with the increase of laser intensity in Figs. 4(a), 4(c), and 4(e). Note that the component of the $3\sigma_g$ orbital in $\Psi_{2\sigma_u}(\mathbf{r},t)$ in Fig. 5(a) is similar to that of the $2\sigma_u$ orbital in $\Psi_{3\sigma_g}(\mathbf{r},t)$ in Fig. 5(b). This is because the single-photon resonant transition occurs here and the maximum difference between them at the same time is around 0.02, which is too small to be distinguished in the figure. [It also occurs for the component of $2\sigma_u$ in Fig. 5(a) and the population of $3\sigma_g$ in Fig. 5(b).] In Fig. 5(c) the population of the $1\pi_u$ state remains nearly unchanged during the pulse due to its weak coupling with unoccupied orbitals.

Now let us return to Fig. 3. Another surprise is that it is harder to remove the electrons in $3\sigma_g$ (HOMO-1) and $2\sigma_u$ (HOMO-2) than in $1\pi_u$ (HOMO) at low laser intensity [see Fig. 3(a)], while the ionization of the electrons from $3\sigma_g$ and $2\sigma_u$ overtakes that from $1\pi_u$ at high laser intensities

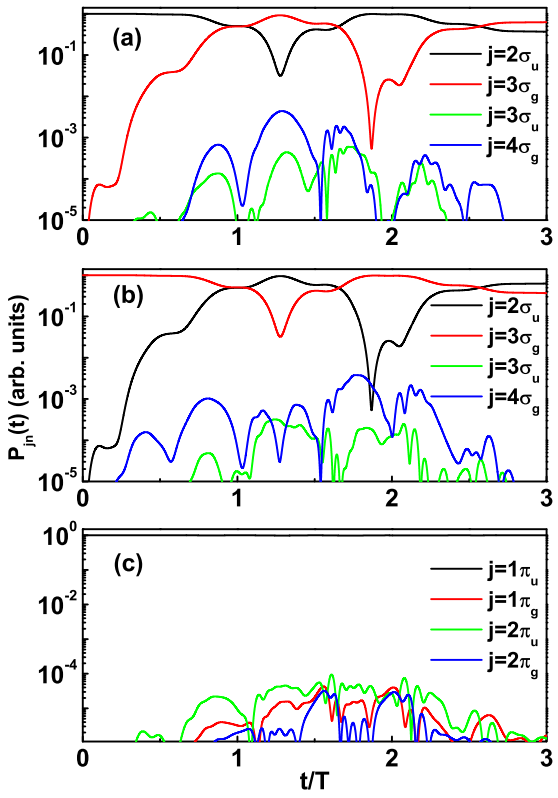

FIG. 5. (Color online) Components of occupied and unoccupied orbitals in time-dependent orbitals for $E_0 = 0.05$ a.u. ($I = 88$ TW/cm^2) with an 800-nm wavelength: (a) $n = 2\sigma_u$, (b) $n = 3\sigma_g$, and (c) $n = 1\pi_u$.

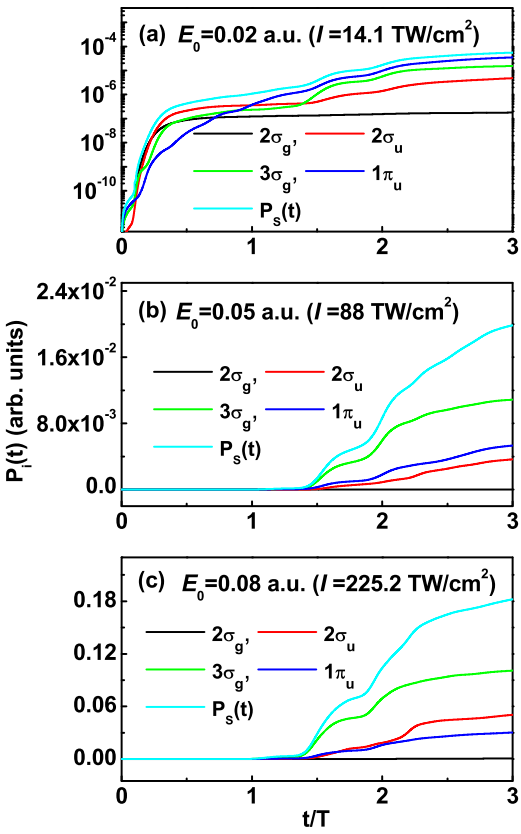

FIG. 6. (Color online) Probabilities of the electron ionized from the i shell $P_i(t)$ and the total ionization probability $P_S(t)$ with an increasing 400-nm laser field. Note that the probabilities are depicted in logarithmic form in (a). For visual convenience, the curves in (b) and (c) are plotted in linear form and the ionization starts at $t = 0$.

[see Figs. 3(b) and 3(c)]. For low laser intensity ($E_0 = 0.02$ a.u.), the Keldysh parameter is $\gamma = 2.56$ for the $1\pi_u$ electron ($\gamma = \sqrt{E_b/2U_p}$, where E_b is the binding energy of the electron and $U_p = E_0^2/4\omega^2$ is its ponderomotive energy in a laser field); the ionization is mainly determined by the binding energy, so the $1\pi_u$ electron is easier to detach than $2\sigma_u$ and $3\sigma_g$ electrons. As the laser intensity increases to $E_0 = 0.05$ and 0.08 a.u., the ionization process approaches the tunneling regime. The distribution of the electron cloud plays an important role in the ionization dynamics. For $2\sigma_u$ and $3\sigma_g$ orbitals, the electron density distributions are parallel to the direction of laser polarization [see Fig. 2], so the electrons in $2\sigma_u$ and $3\sigma_g$ are easier to ionize than the $1\pi_u$ orbital in which the electron density is distributed away from the internuclear axis. Recently, the enhancement of the ionization of the inner electron was attributed to the extended tail of the wave function for the inner orbitals parallel to the direction of the laser field in Ref. [47].

Moreover, it is interesting to note that the binding energy of $1\pi_u$ electrons increases with time for the highest intensity considered here [see Fig. 4(f)]. This is because the ionization of $2\sigma_u$ and $3\sigma_g$ electrons, which is much more pronounced for $E_0 = 0.08$ a.u., reduces the screening for the $1\pi_u$ electrons. This effect is similar to the antiscreening effect from the dynamical core polarization in [29,30]. In Fig. 4(f) it can be seen that the binding energy of the $2\sigma_g$ orbital also increases quickly after $t = T$ because the total ionization probability increases rapidly after $t = T$, which results in weaker screening for the remaining $2\sigma_g$ electrons and thus the $2\sigma_g$ electrons are bound more tightly.

B. Laser field: 400 nm

As we have described above, the similar ionization probabilities of the $2\sigma_u$ and $3\sigma_g$ electrons at the end of the pulse in 800-nm laser fields originates from the single-photon transition between two orbitals. In order to check this mechanism, we also investigate the ionization dynamics of C_2H_2 in the laser field for a 400-nm central wavelength with different laser intensities. We plot the probabilities of the electron ionized from the occupied orbitals and the total ionization probabilities in Fig. 6. Compared with the 800-nm simulations in Fig. 3, there are some interesting differences in Fig. 6.

First of all, it is noteworthy that the ionization probabilities of $2\sigma_u$ electrons are smaller than those of $3\sigma_g$ electrons in Fig. 6. To better understand the change of the ionization of the electrons from occupied orbitals in 400-nm laser fields, we also plot the components of time-independent orbitals $2\sigma_u$ and $3\sigma_g$ in the time-dependent orbital $\Psi_{2\sigma_u}(\mathbf{r},t)$ and time-varying orbital energies in Fig. 7. As described above, it is harder to detach $2\sigma_u$ electrons than $3\sigma_g$ electrons for the following reasons. First, the binding energy of the $2\sigma_u$ electron is bigger

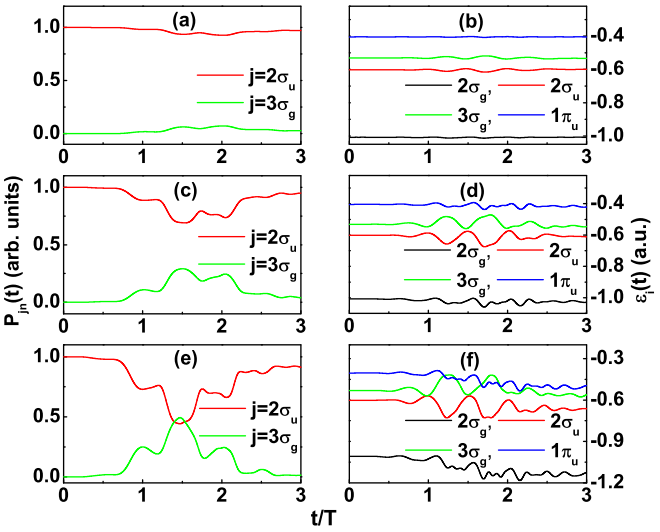

FIG. 7. (Color online) Plot of $P_{jn}(t)$ and orbital energies $\varepsilon_i(t)$ with an increasing 400-nm laser field: (a) and (b) $E_0 = 0.02$ a.u. ($I = 14.1$ TW/cm^2), (c) and (d) $E_0 = 0.05$ a.u. ($I = 88$ TW/cm^2), and (e) and (f) $E_0 = 0.08$ a.u. ($I = 225.2$ TW/cm^2). Note that $n = 2\sigma_u$ in (a), (c), and (e).

than that of the $3\sigma_g$ electron (see Table I). Second, $\omega = 0.114$ a.u. (400 nm) is much bigger than the energy gap $\Delta E = 0.07$ a.u. between the $2\sigma_u$ and $3\sigma_g$ shells, so the single-photon resonant transition is significantly suppressed compared to the 800-nm laser field, and the coupling between the $2\sigma_u$ and $3\sigma_g$ shells is much weaker [see Figs. 7(a), 7(c), and 7(e)] than those in Fig. 4 at the same laser intensity. Accordingly, the energies of the $2\sigma_u$ and $3\sigma_g$ orbitals change less [see Figs. 7(b), 7(d), and 7(f)] than those in Fig. 4 for the same laser intensity.

In addition, similar to the 800-nm calculations, the $1\pi_u$ electron is the easiest to remove for low intensity ($E_0 = 0.02$ a.u.) [see Fig. 6(a)] due to its small binding energy. As the laser intensity increases, since the charge distribution of the $3\sigma_g$ orbital is parallel to the laser polarization direction, which has an impact on the ionization dynamics, the ionization of the $3\sigma_g$ electrons surpasses that of the $1\pi_u$ electron at the end of the pulse [Fig. 6(b)]. For $E_0 = 0.08$ a.u., the ionization of the $2\sigma_u$ electron [Fig. 6(c)] overtakes that of the $1\pi_u$ electron for the same reason. Finally, the ionization of the $2\sigma_u$ and $3\sigma_g$ electrons leads to weaker screening for $1\pi_u$ electrons, which gives rise to the decrease of $1\pi_u$ orbital energies as a function time [see Fig. 7(f)].

IV. CONCLUSION AND OUTLOOK

In this article we developed a three-dimensional TDHF approach to study multielectron ionization dynamics of the C_2H_2 molecule in intense few-cycle laser fields. The wave functions were expanded by the combination of B splines and FEDVR bases to appropriately handle bound states and continuum states and our results obtained by static Hartree-Fock calculations are in good agreement with the reference values. First, we analyzed the coupling of inner shells in strong laser fields with different wavelengths. For the 800-nm laser pulse, the mixing of $2\sigma_u$ and $3\sigma_g$ orbitals becomes stronger when the peak electric field increases from $E_0 = 0.02$ to 0.08 a.u. due to the single-photon transition between the $2\sigma_u$ and $3\sigma_g$ orbitals. This leads to similar ionization probabilities of $2\sigma_u$ and $3\sigma_g$ electrons. For the 400-nm laser pulse, the laser frequency is much larger than the energy gap between the $2\sigma_u$ and $3\sigma_g$ orbitals, so the coupling of the $2\sigma_u$ and $3\sigma_g$ orbitals is weak and the ionization probability of the $2\sigma_u$ electron is significantly less than that of the $3\sigma_g$ electron due to its relatively large ionization potential. Second, calculations show that the ionization of inner electrons will exceed that of the electrons in the HOMO at high laser intensities, which may be attributed to the fact that, at high intensity, the ionization process approaches the tunneling regime in which the spatial distribution of orbitals plays an increasingly important role. Third, it was found that, at high intensities, the binding of the $1\pi_u$ electrons (the HOMO) becomes tighter with the ionization process, which can be ascribed to large probabilities for the electrons removed from inner shells, which reduces the screen effect of the inner electrons on the HOMO electrons. Since the probabilities of the electrons removed from inner shells show a dependence on laser intensities and wavelengths and the orbital density distributions are different for inner electrons, measurements of photoelectron angular distributions may be carried out to explore the inner-shell resonant enhancing ionization phenomena with varying laser intensities and wavelengths in experiments. The above-mentioned phenomena, the inner-orbital single-photon resonant transition and the tighter binding of electrons in the HOMO due to the ionization of inner electrons, provide a further understanding of the molecular ionization process beyond the single-active-electron approximation. The present approach may be extended to investigate the multielectron orientation ionization behavior of linear molecules exposed to intense laser fields [29,33,48].

ACKNOWLEDGMENTS

S.-L.H. acknowledges Professor X. B. Bian and Dr. X. L. Hao for their helpful discussions. This work was partially supported by the National Basic Research Program of China (Grants No. 2013CB922200 and No. 2011CB808102), the National Natural Science Foundation of China (Grants No. 11274348, No. 11374366, No. 11274050, No. 11334009, and No. 11425414), and the China Postdoctoral Science Foundation Grant No. 2014M560921.

[1] F. Krausz and M. Ivanov, Rev. Mod. Phys. **81**, 163 (2009).
[2] M. Drescher *et al.*, Nature (London) **419**, 803 (2002).
[3] M. Schultze *et al.*, Science **328**, 1658 (2010).
[4] H. Akagi *et al.*, Science **325**, 1364 (2009).
[5] C. Y. Wu, H. Zhang, H. Yang, Q. H. Gong, D. Song, and H. M. Su, Phys. Rev. A **83**, 033410 (2011).
[6] X. H. Xie *et al.*, Phys. Rev. Lett. **109**, 243001 (2012).

[7] D. Mathur, K. Dota, A. K. Dharmadhikari, and J. A. Dharmadhikari, Phys. Rev. Lett. **110**, 083602 (2013).
[8] D. G. Lappas *et al.*, J. Phys. B **29**, L619 (1996).
[9] M. S. Pindzola, F. Robicheaux, and P. Gavras, Phys. Rev. A **55**, 1307 (1997).
[10] R. Panfili, J. H. Eberly, and S. L. Haan, Opt. Express **8**, 431 (2001).
[11] D. Bauer, Phys. Rev. A **56**, 3028 (1997).
[12] H. T. Yu, T. Zuo, and A. D. Bandrauk, Phys. Rev. A **54**, 3290 (1996).
[13] R. Nepstad, T. Birkeland, and M. Førre, Phys. Rev. A **81**, 063402 (2010).
[14] Z. Zhang, L.-Y. Peng, M.-H. Xu, A. F. Starace, T. Morishita, and Q. H. Gong, Phys. Rev. A **84**, 043409 (2011).
[15] J. Parker, K. T. Taylor, C. W. Clark, and S. Blodgett-Ford, J. Phys. B **29**, L33 (1996).
[16] E. Dehghanian, A. D. Bandrauk, and G. L. Kamta, Phys. Rev. A **81**, 061403 (2010).
[17] X. Chu and S.-I. Chu, Phys. Rev. A **64**, 063404 (2001).
[18] M. A. L. Marques *et al.*, *Time-Dependent Density Functional Theory* (Springer, Berlin, 2006).
[19] D. A. Telnov and S.-I. Chu, Phys. Rev. A **80**, 043412 (2009).
[20] S. I. Chu, J. Chem. Phys. **123**, 062207 (2005).
[21] L. A. A. Nikolopoulos, T. K. Kjeldsen, and L. B. Madsen, Phys. Rev. A **76**, 033402 (2007).
[22] K. C. Kulander, Phys. Rev. A **36**, 2726 (1987).
[23] N. A. Nguyen and A. D. Bandrauk, Phys. Rev. A **73**, 032708 (2006).
[24] N. E. Dahlen and R. van Leeuwen, Phys. Rev. A **64**, 023405 (2001).
[25] H. Eshuis, G. G. Balint-Kurti, and F. R. Manby, J. Chem. Phys. **128**, 114113 (2008).
[26] E. Lötstedt, T. Kato, and K. Yamanouchi, Phys. Rev. A **85**, 041402 (2012).
[27] E. Lötstedt, T. Kato, and K. Yamanouchi, Phys. Rev. A **86**, 023401 (2012).
[28] E. Lötstedt, T. Kato, and K. Yamanouchi, J. Chem. Phys. **138**, 104304 (2013).
[29] B. Zhang, J. M. Yuan, and Z. X. Zhao, Phys. Rev. Lett. **111**, 163001 (2013).
[30] Z. X. Zhao and J. M. Yuan, Phys. Rev. A **89**, 023404 (2014).
[31] J. Rapp and D. Bauer, Phys. Rev. A **89**, 033401 (2014).
[32] S. L. Hu, Z. X. Zhao, and T. Y. Shi, Int. J. Quantum Chem. **114**, 441 (2014).
[33] S. L. Hu, Z. X. Zhao, and T. Y. Shi, Chin. Phys. Lett. **30**, 103103 (2013).
[34] T. N. Rescigno and C. W. McCurdy, Phys. Rev. A **62**, 032706 (2000).
[35] X. X. Guan, K. Bartschat, and B. I. Schneider, Phys. Rev. A **83**, 043403 (2011).
[36] D. J. Haxton, K. V. Lawler, and C. W. McCurdy, Phys. Rev. A **83**, 063416 (2011).
[37] C. W. McCurdy, M. Baertschy, and T. N. Rescigno, J. Phys. B **37**, R137 (2004).
[38] Y. X. Zhang, Q. Liu, and T. Y. Shi, J. Phys. B **45**, 085101 (2012).
[39] S. Kang, J. Li, and T. Y. Shi, J. Phys. B **39**, 3491 (2006).
[40] S. F. Zhao, C. Jin, A. T. Le, T. F. Jiang, and C. D. Lin, Phys. Rev. A **80**, 051402(R) (2009).
[41] B. Zhang, J. M. Yuan, and Z. X. Zhao, Phys. Rev. A **85**, 033421 (2012).
[42] H. Bachau, E. Cormier, P. Decleva, J. E. Hansen, and F. Martín, Rep. Prog. Phys. **64**, 1815 (2001).
[43] M. J. Frisch *et al.*, GAUSSIAN *03* (Gaussian Inc., Pittsburgh, 2003).
[44] T. K. Kjeldsen, L. B. Madsen, and J. P. Hansen, Phys. Rev. A **74**, 035402 (2006).
[45] X. B. Bian, L. Y. Peng, and T. Y. Shi, Phys. Rev. A **77**, 063415 (2008).
[46] W. Demtröder, *Laser Spectroscopy* (Springer, Berlin, 2002).
[47] A. Russakoff, S. Bubin, X. H. Xie, S. Erattupuzha, M. Kitzler, and K. Varga, Phys. Rev. A **91**, 023422 (2015).
[48] X. H. Xie *et al.*, Phys. Rev. Lett. **112**, 163003 (2014).